An investigation of the mechanisms causing large-amplitude wind-induced vibrations in stay cables using unsteady surface pressure measurements

Mctavish, Sean; Raeesi, Arash; D'Auteuil, Annick; Yamauchi, Kunihiro; Sato, Hiroshi

Publisher's version / Version de l'éditeur:
https://doi.org/10.1016/j.jweia.2018.10.004
Journal of Wind Engineering and Industrial Aerodynamics, 183, pp. 19-34, 2018-10-19

Journal of Wind Engineering & Industrial Aerodynamics 183 (2018) 19–34

Contents lists available at ScienceDirect

Journal of Wind Engineering & Industrial Aerodynamics

journal homepage: www.elsevier.com/locate/jweia

An investigation of the mechanisms causing large-amplitude wind-induced vibrations in stay cables using unsteady surface pressure measurements

Sean McTavish [a,*], Arash Raeesi [a], Annick D'Auteuil [a], Kunihiro Yamauchi [b], Hiroshi Sato [c]

[a] National Research Council Canada, Ottawa, Canada
[b] IHI Corporation, Yokohama, Japan
[c] IHI Infrastructure Systems Co., Ltd, Osaka, Japan

ARTICLE INFO

Keywords:
Stay cable
Dry galloping
Wind-induced vibration
Damping
Wind tunnel

ABSTRACT

Dry galloping has been observed on in-service bridges and has been reproduced in several wind tunnel experiments of inclined stay cables. In certain cases, the large-amplitude vibrations caused by dry galloping could not be mitigated with damping levels specified by the Post Tensioning Institute (PTI). Wind tunnel investigations were conducted for IHI Corporation on a 1:1 scale sectional model of an inclined bridge stay cable in the 3 m × 6 m Wind Tunnel at the National Research Council Canada in 2015. The purpose of the investigation was to reproduce large amplitude cable galloping, which had been observed at an existing cable-stayed bridge in Japan. The experiment was designed to investigate the influence of different damping levels and the ability of a 5 mm-diameter helical fillet to mitigate dry cable vibrations. The current work identified several important factors that contributed to dry galloping and large-amplitude cable motions. It was shown that the physical mechanisms leading to the onset of large-amplitude motion in the critical and supercritical Reynolds number regimes are distinct. In the critical Reynolds number regime, the drop in drag, increase in lift, and fluctuations in the laminar separation bubbles along the cable destabilize the low pressure lobes, allowing the changes in pressure along the cable to become synchronized with the cable motion in a highly-correlated manner. This type of galloping could not be mitigated with damping greater than that required by the PTI. At high Reynolds numbers, the boundary layer state changed and was associated with the upstream movement of the separation point and an asymmetric pressure distribution, Kármán vortex shedding re-emerged and appeared to combine with low-frequency variations to induce large-amplitude motion. The large-amplitude motion at high Reynolds numbers could be mitigated with additional damping.

1. Introduction

Cable-stayed bridges have been used in increasingly diverse situations over the past three decades. Stay cables are made with a bundle of steel cables that are fed through a high density polyethylene (HDPE) tube. The use of HDPE tubes has some drawbacks in regards to the aerodynamic characteristics of stay cables. The smooth surface of the tube can lead to rain-wind-induced vibrations. Enclosing the steel strands in an HDPE tube also reduces the mass per cross-sectional area of the stay cables which results in an unfavourable mass-damping relationship with respect to wind-induced vibrations. Additionally, dry galloping can be induced at certain wind speeds due in part to the smooth surface of the tube and the inclined attitude of the stays. Dry galloping refers to large amplitude (can be on the order of several times the cable diameter) and low frequency (on the order of 1 Hz) vibrations of a stay cable that occur in the absence of rain, ice, or snow.

The potential sensitivity of stay cables to wind-induced vibrations can be reduced by increasing the structural damping of the stays, by altering the surface of the HDPE tube with a geometric treatment such as a helical fillet or a pattern-indented surface, or by installing cross-ties between the stays (?). Although such strategies have been successful in many instances, the mechanisms leading to dry galloping on a smooth cable are not fully understood by the scientific community. Dry galloping has been observed on in-service bridges (Yamauchi et al., 2016) and has been reproduced in several wind tunnel experiments of inclined stay cables (Cheng et al., 2008; Nikitas et al., 2009; Larose and D'Auteuil, 2014; Matsumoto et al., 2017). In certain cases, the large-amplitude vibrations caused by dry galloping could not be mitigated with damping levels

* Corresponding author.
E-mail address: sean.mctavish@nrc-cnrc.gc.ca (S. McTavish).

https://doi.org/10.1016/j.jweia.2018.10.004
Received 12 July 2018; Received in revised form 6 September 2018; Accepted 2 October 2018
Available online 19 October 2018

specified by the Post-Tensioning Institute (PTI Guide Specification, 2012).

Dry galloping has been linked to several flow features that become apparent in the critical Reynolds number regime. The critical Reynolds number regime in flow past cylinders is typically accompanied by drastic changes in the drag and lift force coefficients in response to relatively small changes in the Reynolds number. The variation in forces for a classical smooth cylinder is characterized by a drop in the drag coefficient with increasing Reynolds number (referred to as the drag crisis) and an increase in the absolute value of the lift coefficient. For a smooth circular cylinder, the critical Reynolds number range typically emerges at a Reynolds number greater than 2.5×10^5. Factors such as surface roughness and turbulence in the freestream can promote the emergence of the critical regime at lower Reynolds numbers.

The terminology of Zdravkovich (1997) is used in this article to describe the different flow regimes that can be present on an inclined cable. For a smooth circular cylinder, Zdravkovich described several distinct regimes that characterize the transition in the boundary layer (TrBL). In the TrBL regimes, the transition from laminar to turbulent flow for a smooth circular cylinder will occur in the boundary layer or in a separation bubble. The lift and drag coefficients experience large variations between a Reynolds (*Re*) number of 10^5 and 10^6, as shown in Fig. 1. Many engineering structures, including stay cables, operate in the range of Reynolds numbers that correspond to the TrBL regimes.

The TrBL behaviour is demarcated into five regimes (TrBL0 to TrBL4) that are characterized by their respective transition and separation behaviour as a function of Reynolds number. The change in separation behaviour for TrBL0 to TrBL3, which correspond to the flow regimes observed in the current experiment, is described in Fig. 2. In the TrBL0 regime, turbulent separation (*T*) occurs from both sides of the cylinder, resulting in a large drag coefficient and early flow separation. In the TrBL1 regime, the laminar boundary layer will separate (*L*) and reattach to the surface of the cylinder before turbulent separation occurs further downstream. The area between the laminar separation and the turbulent reattachment is described as a laminar separation bubble. This results in a large suction lobe and occurs only on one side of the cylinder in the TrBL1 regime. The low pressure suction lobe can switch from one side of the cylinder to the other (referred to as state jumps) or can appear intermittently on one side of the cylinder (defined as bi-stable flow) (Benidir et al., 2015). In the TrBL2 regime, a laminar separation bubble is present on both sides of the cylinder. The reattachment of the flow on both sides of the cylinder results in a significant reduction in the drag coefficient. The TrBL1 and TrBL2 regimes are highly sensitive to Reynolds number and the pressure field can fluctuate between the two regimes. The TrBL3 regime typically occurs at Reynolds numbers above 500,000 for a smooth cylinder and is characterized by a forward shift in the turbulent separation location and a larger wake. The TrBL1 and TrBL2 regimes occur in the critical Reynolds number regime and the TrBL3 occurs at Reynolds numbers that are assumed to be in the supercritical Reynolds number regime.

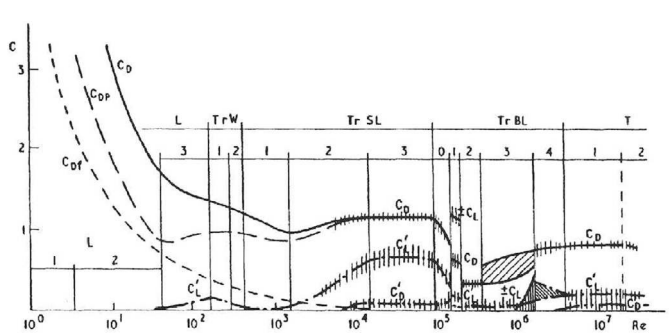

Fig. 1. Lift and drag coefficients as a function of Reynolds number, from Zdravkovich (1997).

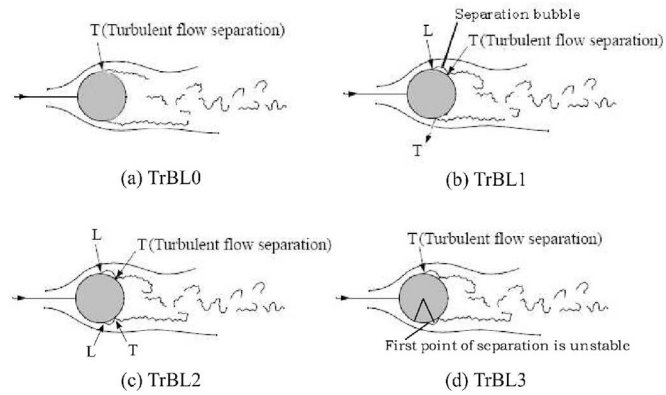

Fig. 2. Characteristics of the TrBL flow regimes. Adapted from D'Auteuil (2010) and ESDU (1971).

Wind tunnel investigations were conducted for IHI Corporation (IHI) on a 1:1 scale sectional model of an inclined stay cable in the 3 m × 6 m Wind Tunnel at the National Research Council Canada (NRC) in 2015. The purpose of the investigation was to reproduce and mitigate large amplitude cable galloping, which had been observed at an existing cable-stayed bridge in Japan. The experiment was designed to investigate the influence of different damping levels on the cable response, and the ability of a 5 mm-diameter helical fillet to mitigate dry cable vibrations. The test systematically evaluated the effect of cable shape, cable-wind plane, damping levels, and surface treatments in a setup where unsteady pressure measurements were synchronized with displacements. The setup therefore allowed dynamic forces and spanwise variations in surface pressures to be associated with the cable response. The dynamic response of the cable as a function of its cross-sectional shape, damping levels, and the helical fillet surface treatment was published previously by Yamauchi et al. (2016).

The current manuscript provides a detailed investigation of the unsteady surface pressure data at several damping levels and in the critical and supercritical Reynolds number regimes to explain the two distinct cable vibration phenomena that were observed. The article investigates dry galloping, which is characterized by large, unbounded oscillations in the critical Reynolds number regime, as well as large-amplitude vibration, which was observed herein as bounded oscillations at supercritical Reynolds numbers. The article describes the experimental setup, presents the cable vibration behaviour that was encountered, evaluates the unsteady pressures and forces associated with vibrations encountered in different flow regimes, and proposes several factors that contributed to dry galloping.

2. Experimental setup

The test campaign was carried out in the NRC 3 m × 6 m Wind Tunnel in Ottawa, Canada. This large open circuit wind tunnel has a 7.9 m diameter 16-blade fan that draws outdoor air and pushes it through a large settling chamber followed by a 6:1 contraction ratio. The fan is fitted with a set of anti-swirl stators and the settling chamber has a set of fine mesh screens to keep flow turbulence to a minimum. The test section is 3.05 m wide, 6.1 m high, and 12.2 m long. The test section is followed by a diffuser with a 90° bend and the tunnel exhausts directly outdoors. The wind tunnel has a nominal turbulence intensity of 0.4%–0.75% at above a test section wind speed of 14 m/s and a nominal turbulence intensity of 0.7%–1.2% for a test section wind speed between 8 and 14 m/s. These turbulence intensity values are indicative of the flow conditions at the tunnel centreline. The turbulence intensity distribution over the length of the cable was not characterized in this experiment.

Fig. 3 shows a view of the smooth IHI cable model installed in the wind tunnel. The suspension rig that has been used for previous inclined cable experiments in the same test facility, described in detail in Larose

Fig. 3. Smooth cable model in the NRC 3 m × 6 m Wind Tunnel, looking upstream.

and D'Auteuil (2014), was also used for the present study. The model was supported by a set of springs in two orthogonal directions. The upper end of the model protrudes through the ceiling of the test section and was connected to an upper suspension rig on the roof of the wind tunnel. The mass of the cable was supported by a steel wire suspended from the ceiling of the building. The lower end of the model and the lower rig were fully immersed in the flow. The rig has the capability to rotate the cable about its own axis without a rotation of the spring plane. This capability was utilized to verify the effect of deviations in the cable shape on the cable response.

The parameters that are known to influence inclined cable galloping (mass, damping, geometry) were simulated adequately at full-scale in the present study and were designed to reflect conditions at which galloping had been observed on a bridge in service in Japan. The cable model had an outer diameter of 219 mm, a length of 6687 mm, and was composed of concentric steel and HDPE tubes. The aspect ratio of the model based on its exposed length and the cable diameter was 26. The suspended mass was 493 kg, which corresponds to a mass per unit length of 73.7 kg/m, which is consistent with full-scale stay cables. The cable oscillated with a frequency of approximately 1.24 Hz in sway and 1.25 Hz in heave.

The geometry of a stay cable and the yaw angle of the wind are represented in Fig. 4. Although stay cable arrays are not always oriented in the vertical plane, it has been assumed in this experiment that the cable axis and the bridge axis lie in a vertical plane and the cable axis forms a geometric cable angle (θ) relative to the horizontal bridge axis. The wind yaw angle (β) is defined in the horizontal plane relative to the

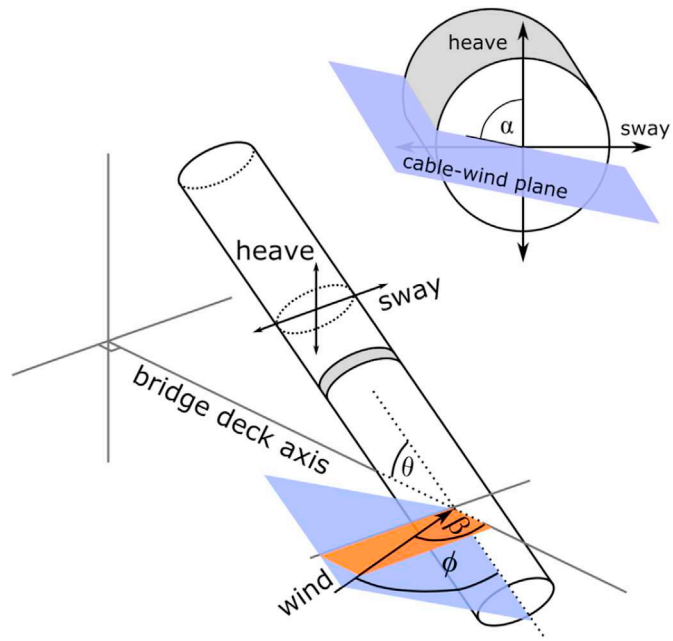

Fig. 4. Definition of the wind direction (β), the geometric cable angle (θ), the cable-wind angle (ϕ), and the vibration axis rotation angle (α).

bridge axis. The wind vector and the cable axis form the cable-wind angle (ϕ). The orientation of the resulting cable-wind plane relative to the heave and sway vibration axes of the cable is shown in Fig. 4 and is characterized by the angle α.

It has been standard practice in previous experiments to assume that the orientation of the cable relative to gravity is not important for the aerodynamic behaviour of a dry cable (Nikitas et al., 2009). The cable-wind angle and the three-dimensional geometry of an inclined cable represented in Fig. 4 can then be transformed into equivalent conditions in a wind tunnel following the equations derived by Cheng et al. (2008). The model in the wind tunnel has an inclination angle equal to the cable-wind angle (ϕ) and has its principal vibration axes (the spring plane in the experimental setup) rotated relative to the cable-wind plane (α).

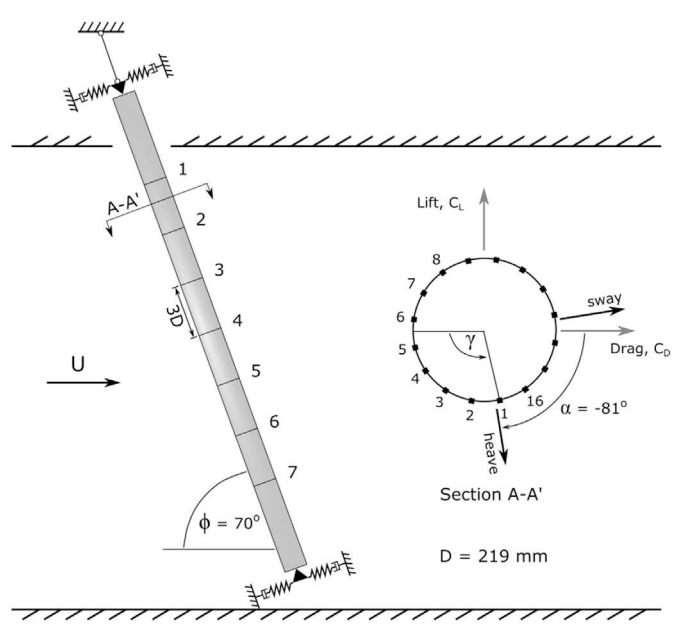

Fig. 5. Schematic of the IHI cable model inclined at 70° in the wind tunnel.

The arrangement of the IHI cable in the wind tunnel is detailed in Fig. 5. The cable-wind angle (inclination in the wind tunnel) and principal vibration axis rotation angle were selected to represent the field conditions from an existing bridge site. The cable-wind angle (ϕ) and spring rotation angle (α) relate to the stay cable geometric inclination in the field (θ) and flow yaw angles (β) through the following equations:

$$\cos\phi = \cos\beta \cdot \cos\theta \tag{1}$$

$$\tan\alpha = \frac{\tan\beta}{\sin\theta} \tag{2}$$

Using these relationships, a wind tunnel model inclination angle of $\phi = 70^\circ$ and a spring rotation of $\alpha = -81^\circ$ correspond to a stay cable inclination in the field of $\theta = 24^\circ$ and yaw angle of $\beta = 68^\circ$.

The dynamic rig also has the ability to adjust the angle of the cable about its own axis (γ), independent of the spring rotation angle. The axial rotation angle is defined in Fig. 5 and corresponds to 0° when pressure tap 1 is located at stagnation. A study of the axial rotation of the cable was conducted during the experiment. The results of the axial rotation study demonstrated that the cable vibration was dependent on the cable shape and the selected angle had the largest-amplitude motion of the cases that were considered (Yamauchi et al., 2016). The results in this manuscript were based on a cable axis rotation angle of $\gamma = 102^\circ$ as shown in Fig. 5, but an additional set of results with $\gamma = -110^\circ$ were used to confirm the mechanisms contributing to cable vibrations.

A three-dimensional scan of the model identified distinct regions of eccentricity in the diameter, with lobes and valleys along the span of the model and greater deviations near the lower half of the model. The deviations from a circle are shown at three spanwise locations in Fig. 6. The deviation plot shows the orientation of the cable relative to pressure tap 1 and the freestream wind speed. Note that the deviations in Fig. 6 have been magnified to show the detail of the lobes, and the largest observed deviation at each spanwise ring is indicated on the corresponding ring outline. The largest observed deviation was equivalent to 0.25% of the mean diameter. This deviation is smaller than deviations observed on in-service cables and in other experiments, which are typically on the order of 1% of the cable diameter (Larose and D'Auteuil, 2014; Benidir et al., 2015). The surface roughness of the model was measured using a portable roughness tester. The mean roughness parameter (R_a) of the model was measured at three spanwise locations on the model and varied from 0.836 μm to 1.143 μm. This corresponds to roughness-to-diameter ratios ranging from 3.82E-6 to 5.22E-6. The range of roughness values is consistent with measurements conducted on stay cables at the Øresund bridge site (??).

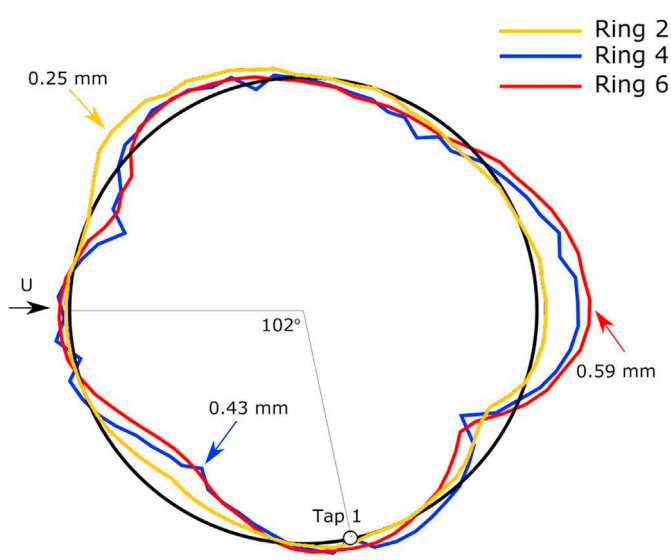

Fig. 6. Deviations on the cable model at three spanwise locations. Note that deviations have been magnified to show detail. The largest deviation at each spanwise location is indicated by an arrow with the corresponding colour. (For interpretation of the references to colour in this figure legend, the reader is referred to the Web version of this article.)

2.1. Displacement measurements

The sway and heave motion at the extremities of the cable model were measured with laser displacement transducers (Wenglor model CP35MHT80, 0.05 mm resolution). Four laser displacement sensors were used, with one sensor in heave and one sensor in sway at each end of the model. The laser displacement signal was digitally low-pass filtered with a cut-off frequency of 30 Hz during data reduction. The heave vector shown in Fig. 5 indicates a direction based on a spring plane rotation of −81°. However, the heave displacements that will be shown in the results section have been multiplied by −1 so that a positive heave displacement corresponds more intuitively to the positive lift coefficient direction shown in Fig. 5.

2.2. Pressure measurements

The IHI cable model was instrumented with 128 pressure taps. The pressure taps were arranged in seven cross-sectional rings that had a spanwise spacing of 3 diameters (D), as identified in Fig. 5. Rings 1 to 3 and 5 to 7 (counting from the top of the cable to the bottom) each contained 16 surface pressure taps with uniform spacing of 22.5°. Ring 4 was centred in the spanwise direction and contained 32 pressure taps with uniform spacing of 11.25°. Two electronic pressure scanners were embedded directly in the stay cable to minimize the length of pneumatic tubing inside the model. It should be noted that Ring 1 was located less than 1D from the hole in the ceiling of the wind tunnel when the model was inclined at 70°. As a result of the wall proximity effects, the pressures for Ring 1 are not included in the current analysis.

The pressure signals from the scanners were synchronized with the laser displacement signals and were acquired at 312.5 Hz for 90 s. The frequency response of the tubing system was measured prior to the experiment to account for the distortion of the pressure signals due to the tubing and the pressure scanner. This procedure was applied to each port on the pressure scanner using pressure tubing of a uniform length. The resulting transfer functions were used to correct the unsteady pressure measurements for magnitude and phase distortions caused by the tubing length and the volume of air inside the transducer.

Due to the inclined geometry and dynamic response of the cable, the pressure coefficients and resulting force coefficient time histories were not corrected for blockage effects. The geometric blockage was calculated to be 5.4% of the test section area based on the exposed frontal area of the cable. The low level of blockage justifies the use of data that are uncorrected for blockage effects.

2.3. Damping

Damping is defined using the damping ratio and the Scruton (Sc) number. The Scruton number is a nondimensional mass-damping parameter that characterizes the relationship between the structural damping and the ratio between an oscillating mass and the displaced mass of air. The Scruton number can be based on the damping ratio as a fraction of critical (Sc_ζ) or damping as a function of the logarithmic decrement (Sc_δ). The two definitions of the Scruton number that are used in literature are defined in Equations (3) and (4), where m is the oscillating mass per unit length, ζ is the damping ratio as a fraction of critical, δ is the logarithmic decrement, ρ is the air density, and D is the cable diameter. The Scruton number based on the logarithmic decrement (Sc_δ) relates to the damping ratio through $\delta = 2\pi\zeta$. The damping level applied to each test configuration in this article will be characterized using the damping ratio as a fraction of critical (Sc_ζ).

$$Sc_\zeta = \frac{m\zeta}{\rho D^2} \tag{3}$$

$$Sc_\delta = \frac{2m\delta}{\rho D^2} \tag{4}$$

The three levels of damping specified in Table 1 were evaluated throughout the experimental campaign. The damping of the cable was determined before each speed sweep using a decay trace. The damping ratio, as a percent of critical, was identified at an amplitude of 10 mm for consistency at the low, medium, and high damping levels.

3. Results

The current results focus on the mechanisms causing vibrations of a smooth cable. The amplitude of the cable response at three damping levels will be presented, followed by an investigation of the mean and unsteady surface pressures in the critical and supercritical Reynolds number regimes, and an investigation of the sectional and overall lift coefficient.

3.1. Cable vibrations at several damping levels

The wind-induced amplitude of the smooth cable at three damping levels is shown in Fig. 7. The motion of the cable was predominantly in the heave direction and so only this degree of freedom is shown below. With low damping ($Sc_\zeta = 1.9$), large amplitude cable galloping was observed in the critical Reynolds number regime that necessitated a reduction of the wind speed and interruption of the tests to prevent damage to the spring suspension rig. When the damping was increased to reach $Sc_\zeta = 6.8$ and $Sc_\zeta = 13.5$, oscillations were present in heave over a narrow band of Reynolds numbers near 270,000. In the high damping case ($Sc_\zeta = 13.5$; 1.1% of critical), oscillations of 20 mm were still observed at $Re = 270{,}000$ (18.5 m/s), demonstrating that galloping on a smooth cable could not be eliminated with this level of damping, which was greater than the level recommended by the Post-Tensioning Institute (PTI). The PTI specifies that damping equivalent to Sc_ζ °>°10 is considered sufficient to mitigate both rain-wind vibration and dry-state cable galloping on a smooth stay cable (PTI Guide Specification, 2012). The current results, however, demonstrated that galloping can occur at even higher damping levels in certain wind conditions, and have highlighted that, given the difficulty of increasing the structural damping level of long stay cables, additional damping alone may not always be sufficient to mitigate dry cable galloping.

In the low damping case, large amplitude motion was again observed at Reynolds numbers above 450,000 (32–35 m/s), although the displacement was bounded at these speeds. The oscillations at high Reynolds numbers that had been observed at the lowest damping level were, however, successfully mitigated with additional damping.

A helical fillet was evaluated during the test program as a countermeasure for dry galloping and is presented in more detail in Yamauchi et al. (2016). Although not shown in Fig. 7, the 5 mm diameter helical fillet successfully attenuated cable vibrations at all damping settings and wind conditions considered in the experiment.

3.1.1. In-test repeatability

The in-test repeatability was evaluated by performing speed sweeps on subsequent test days. The repeatability of the measured amplitude is demonstrated in Fig. 8. The speed sweeps did not have the same resolution near 18 m/s, and so the Day 1 run did not fully capture the peak amplitude due to the use of coarser steps between wind speeds. Nevertheless, both runs identified similar cable response. The repeatability of the setup between two tests conducted in 2011 and the current test conducted in 2015, using the legacy NRC cable model, was demonstrated in Yamauchi et al. (2016).

Table 1
Summary of damping settings in the heave direction for each configuration.

Damping	ζ [% Cr]	Sc_ζ	Sc_δ
Level	heave	heave	heave
Low	0.15	1.9	24
Med	0.54	6.8	85
High	1.08	13.5	170

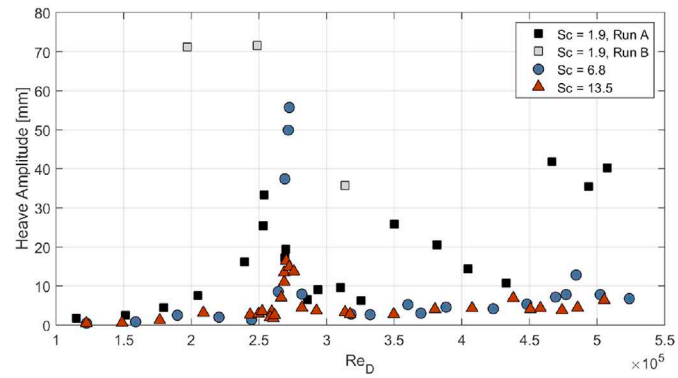

Fig. 7. Effect of damping on the heave amplitude of the cable. The *Run B* data series at $Sc_\zeta = 1.9$ was recorded at the same low damping test condition, but on a separate day.

4. Pressures

The surface pressure data from the current experiment were used to investigate the presence of several flow regimes on the smooth cable, their spanwise variation along the cable, and their relationship to the large-amplitude vibrations observed during the experiment.

4.1. Mean surface pressures

The pressure contours from Ring 4 are presented over a range of wind speeds corresponding to the critical and supercritical Reynolds number regimes in Fig. 9. Four of the tap numbers are identified at each of the seven rings of pressure taps for reference. Positive pressure contours are indicated in red while regions of suction are indicated in blue.

4.1.1. Critical Reynolds number regime

A pressure distribution corresponding to the pre-critical regime (TrBL0 according to the nomenclature of Zdravkovich (1997)) is visible at the lowest Reynolds number shown in Fig. 9. The TrBL1 regime is characterized by the formation of a laminar separation bubble on one side of the cylinder followed by a short reattachment and finally turbulent separation, leading to an asymmetric pressure distribution, the generation of steady across-wind forces and a drop in drag due to a delay

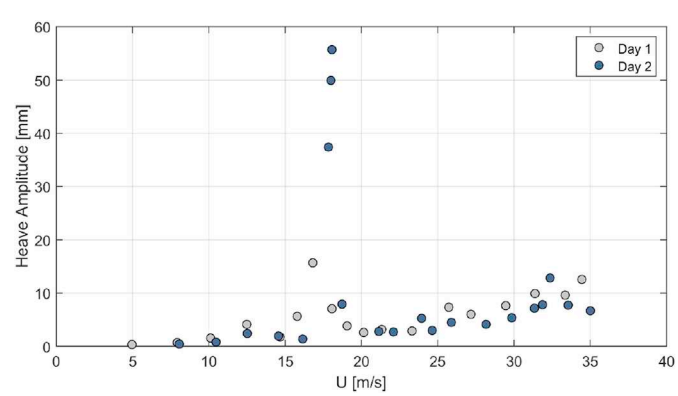

Fig. 8. In-test repeatability of the heave amplitude of the cable. $Sc_\zeta = 6.8$.

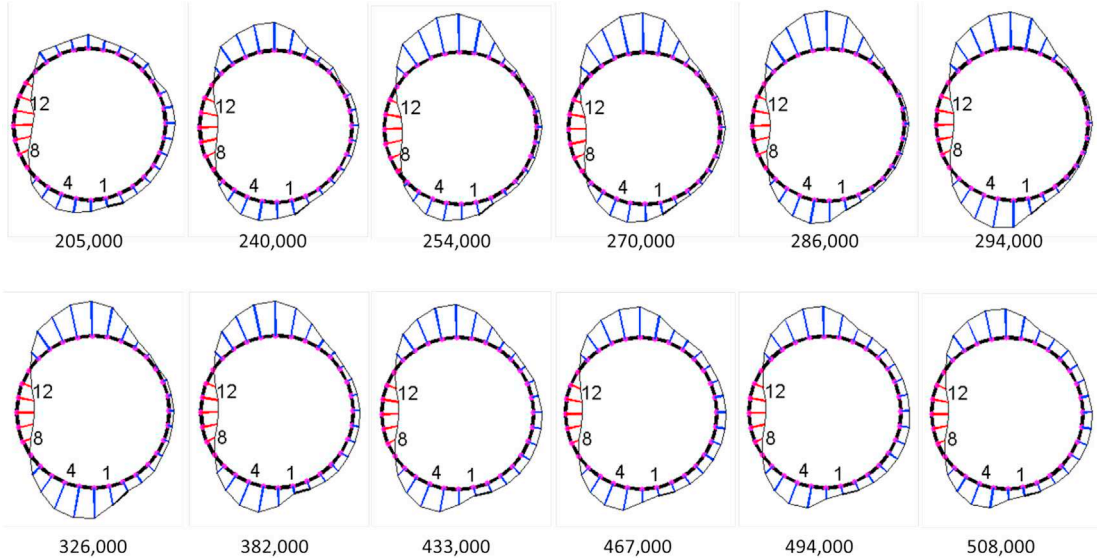

Fig. 9. Mean pressure contours for the mid-span pressure taps (Ring 4) at several Reynolds numbers. $Sc_\zeta = 1.9$.

of the boundary layer separation. The presence of a laminar separation bubble results in a lobe in the low pressure distribution on the side of the cable experiencing the separation and reattachment. The pressure tap distribution was not fine enough to identify the beginning and end of the laminar separation bubble, but the low pressure lobe is an indicator of the bubble's presence. A single separation bubble region was present from Reynolds numbers of 240,000 to 270,000 for Rings 5 and 6 (not shown), after which the low pressure lobe associated with a laminar separation bubble was visible on both sides of the cylinder. This corresponds to the TrBL2 regime, which is associated with a more symmetric pressure distribution and a further drop in drag. The distribution on Ring 4 in the range of Reynolds numbers from 240,000 to 270,000 is asymmetric, with a weak low pressure lobe on the port surface (left side, when looking upstream) surface and a strong low pressure lobe on the starboard surface (right side, when looking upstream). Bi-stable states in the surface pressures can be present during the passage from the TrBL0 to TrBL1 regime or from TrBL1 to TrBL2 regime. It has been suggested that the bi-stable states are linked to the onset of dry-state cable galloping (Benidir et al., 2015), but there has been only limited experimental evidence of this; bi-stable states have been observed on a free-to-respond cable model without vibrations occurring (Larose and D'Auteuil, 2014). The large-amplitude galloping in this experiment occurred near 18 m/s, corresponding to a Reynolds number of approximately 260,000–272,000, and, as will be discussed later, near conditions where bi-stable states were present in some cases but not in others.

The pressure data were subsequently used to investigate the spatial

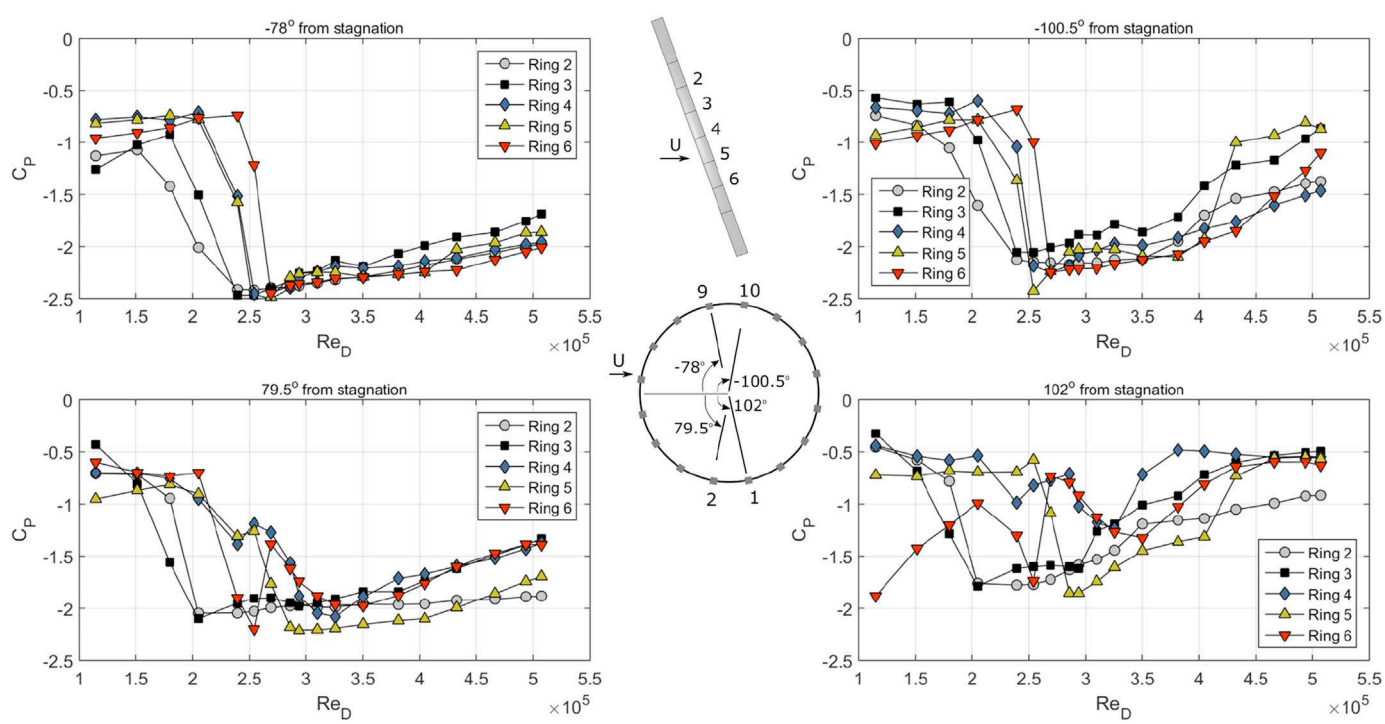

Fig. 10. Mean pressure coefficients as a function of Reynolds numbers at tap locations near separation. The ring numbering convention and labels for selected tap numbers for rings with 16 taps (Rings 2, 3, 5, 6) are shown on the inset schematic. These locations correspond to taps 1, 3, 17, 19 for Ring 4. $Sc_\zeta = 1.9$.

variation in transition along the cable. It has been discussed in Jakobsen et al. (2009) and Nikitas and Macdonald (2015) that pressure distributions at cross-sections located as little as 2 to 4 diameters apart can exhibit different characteristics, indicating different flow regimes. Similar characteristics were found to be present in the current study. The mean pressure coefficients near the separation points from Rings 2 to 6 are plotted as a function of Reynolds number in Fig. 10. Each pair of pressure taps shown in Fig. 10 is roughly symmetric about the vertical-streamwise plane of the cable and angles are defined as positive counter-clockwise when viewed from above. The pressure taps located at -78° and -100.5° from the stagnation point exhibited similar behaviour. The pressure coefficients (C_P) experience a rapid drop from approximately -0.75 to a minimum of -2.5, indicating the formation of a separation bubble on the starboard side of the cable. Interestingly, the drop in C_P occurred at different Reynolds numbers for each ring and seemed to result in a sequential change in the boundary layer state moving downward along the cable axis. The drop in C_P occurred first for Ring 2, located upstream and high on the cable, and occurred last for Ring 6, located near the bottom, downstream extremity. Similar behaviour was also observed for the tests with $Sc_\zeta = 6.8$, and $Sc_\zeta = 13.5$ (not shown in this article). This is consistent with the discussion in Nikitas et al. (2009), which demonstrated that spanwise "cells" of flow can be present along the length of the cable. The variation in C_P (indicating the potential for various states) along the length of the cable can be observed by comparing C_P in the critical Reynolds number regime at the tap located at 79.5°. This is indicative of a level of spanwise three-dimensionality in the mean pressure contours. Rings 2 and 3 exhibited a suction peak at 79.5° that was already present at a Reynolds number of 200,000. Rings 4 and 5 had a more gradual growth in the low pressure lobe with a small amount of instability near $Re = 250{,}000$. Ring 6 experienced a sudden formation in a separation bubble on the port side of the cable at $Re = 254{,}000$. A further small increase in Reynolds number to 270,000 resulted in a reduction in the strength of the low pressure lobe at this location in an average sense, by comparison with the pressure tap located at -78°. Dry galloping was observed on this cable at a Reynolds number of approximately 260,000–272,000, implying that the presence of one or two low pressure lobes, and the transition between the TrBL1 and TrBL2 regimes, were contributing factors in the initiation of the large-amplitude vibrations observed in this case. The pressure coefficients at the tap located 102° from stagnation exhibited more variability than the other taps shown in Fig. 10. The tap located 102° from separation is also near the apex of one of the small lobes on the cable based on the model shape shown earlier in Fig. 6. As a result, the flow separation behaviour may have been more sensitive at this location and the separation point varies along the cable axis.

A high degree of similarity was observed in the mean pressure coefficients at the low and medium damping levels, particularly in the critical Reynolds number regime. As a result of the similarities, the medium damping level case ($Sc_\zeta = 6.8$) will be used during the discussion of the unsteady pressure results in the critical Reynolds number regime below, because the medium damping level permitted sustained operation at a wind speed where large amplitude galloping was observed. This condition resulted in large-amplitude oscillations, but provided enough damping for the vibrations to be bounded, unlike the lower damping case which resulted in growing vibrations. The pressure coefficients from the low damping case ($Sc_\zeta = 1.9$) will be used to discuss the large-amplitude vibrations that were observed in the supercritical Reynolds number regime, since these vibrations were only observed at the lowest of the three damping settings evaluated in the experiment.

4.1.2. Supercritical Reynolds number regime

Following an increase in Reynolds number (382,000 and above), the pressure distributions shown in Fig. 9 became asymmetric, the separation point moved forward, and the base pressure increased, indicating the presence of the onset of the TrBL3 regime. The TrBL3 regime is typically characterized by a forward shift in the separation point, a thickening wake, and an associated increase in drag. The large amplitude, bounded, motion that was observed at high speeds in the present experiment ($Re >$ 433,000) corresponded to the presence of this mean asymmetric pressure distribution. At Reynolds numbers greater than 400,000, the pressure taps at -100.5° and 102° from stagnation showed an increase in C_P in Fig. 10, which is related to a forward shift in the separation point.

4.2. Unsteady pressure coefficients

The discussion in Section 4.1 identified the changing nature of the average pressure contours at the middle ring of pressure taps on the cable and identified that several boundary layer states can be present along the cable at a given Reynolds number. Instantaneous pressure contours are examined in this section to demonstrate the fluctuations in the boundary layer states prior to and during large-amplitude vibrations in the critical and supercritical Reynolds number regimes.

4.2.1. Critical Reynolds number regime

The unsteady pressure contours from the medium damping case ($Sc_\zeta = 6.8$) were investigated in greater detail in the critical Reynolds number regime, since the damping level allowed sustained wind tunnel operation at a dry galloping condition due to the large, but bounded nature of the vibrations. The peak amplitude that had been observed for this case corresponded to a Reynolds number of 272,000 and large-amplitude motion was shown earlier in Fig. 7 to occur only over a narrow band of Reynolds numbers. Instantaneous pressure contours prior to the onset of galloping are shown in Fig. 11. At time t_1, before the onset of galloping, the pressure contours for Ring 3 indicate the presence of a symmetric TrBL2 regime, with low pressure lobes on both sides of the cable. Ring 4 has an asymmetric TrBL2 regime, with a stronger low pressure lobe on the starboard side of the cable. Rings 5 and 6 are in the TrBL1 regime at t_1 and exhibit their single low pressure lobe on opposite sides of the cable. A change in the boundary layer states can be observed by comparing the pressure contours at times t_1 and t_2. The pressure contours at Ring 3 are stable over this time interval, but the level of asymmetry on Ring 4 has increased at t_2. The pressure distribution on Ring 5 alternated between a TrBL1 distribution and an asymmetric TrBL2 distribution. Ring 6 was predominantly in the TrBL1 regime with an intermittent development of a second, weak low pressure lobe on the starboard surface. Even though Rings 5 and 6 show the formation of the opposing second, weak low pressure lobe at the same time in Fig. 11, they were not always formed simultaneously and were not synchronized with motion at $Re = 264{,}000$. Additionally, although there was no evidence of a TrBL1 state jump in the time history prior to galloping for $Sc_\zeta = 6.8$, single laminar separation bubble state jumps were observed on Ring 6

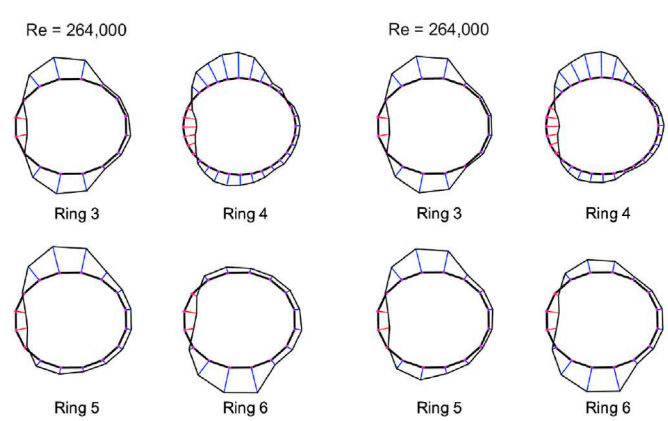

(a) Pressure contours at t_1. (b) Pressure contours at $t_2 = t_1 + 1.39$ s.

Fig. 11. Instantaneous pressure coefficients prior to the onset of galloping. $Sc_\zeta = 6.8$.

before galloping in the low damping case.

Instantaneous pressure contours during a galloping event at a Reynolds number of 272,000 are shown in Fig. 12. The heave amplitude of the cable is shown over approximately one cycle and the pressure contours for Rings 2–7 are shown at three instances in time. It can be observed that the symmetric, TrBL2 distribution for Rings 2 and 3 is constant throughout the cycle. Ring 4 has an asymmetric pressure distribution, with a small increase on the port surface of the cable at the negative peak in displacement. Rings 5 and 6 both alternate between a single laminar separation bubble on one side of the cable and an asymmetric TrBL2 regime. The pressure distribution for Ring 7 experiences large fluctuations, more similar to a TrBL1 regime that fluctuates between TrBL1 and TrBL0. It can be seen in Fig. 12 that the direction of the change in surface pressure of the cable is associated with the direction of the heave displacement of the cable. Rings 4, 5, 6, and 7 all experience larger negative pressures on the port side of the cable at the largest negative heave displacement, during which the cable moves to port. An important observation in Fig. 12 is that the results indicate that several states can be present along the cable during a galloping event and that the same state does not need to be present along the entire cable. It will be demonstrated later in Section 5.2 that an important factor is the level of correlation between the fluctuations at each ring.

4.2.2. Supercritical Reynolds number regime

Unsteady pressure coefficients are shown in Fig. 13 for the conditions in supercritical flow where additional large-amplitude displacements were observed in this experiment. The data shown in Fig. 13 include an extracted time history of pressure coefficients on Ring 5, at taps located at -100.5° and at 102° from stagnation. The pressure coefficients at Ring 5 represented the largest jump in the mean C_P data at $Re = 430{,}000$ shown earlier in Fig. 10. A forward shift in the separation point, a reduction in the suction peak, and an associated increase in drag were observed for the unsteady data and the mean pressure contours in Fig. 13. It is notable that there are no large fluctuations in the unsteady pressures shown in Fig. 13, contrary to what had been observed in the critical Reynolds number regime. In addition to the forward shift in the separation point, consistent with the onset of the TrBL3 regime, the sectional pressure distributions were similar along the length of the cable. Given the different flow regimes present during galloping in the critical Reynolds number regime (Fig. 12) and the vibrations at high Reynolds number (Fig. 13), the triggering mechanism is expected to be different, and this is discussed further in Section 5.

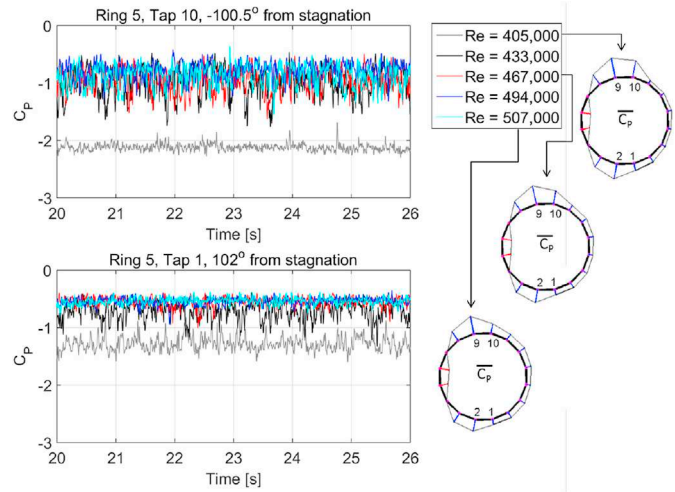

Fig. 13. Instantaneous pressure coefficients for Ring 5 at high Reynolds numbers. $Sc_\zeta = 1.9$. The mean pressure distribution at Ring 5 is also shown for three Reynolds numbers.

5. Lift coefficient

The instantaneous pressure distribution at each ring of pressure taps was integrated to calculate the unsteady lift coefficient acting on each

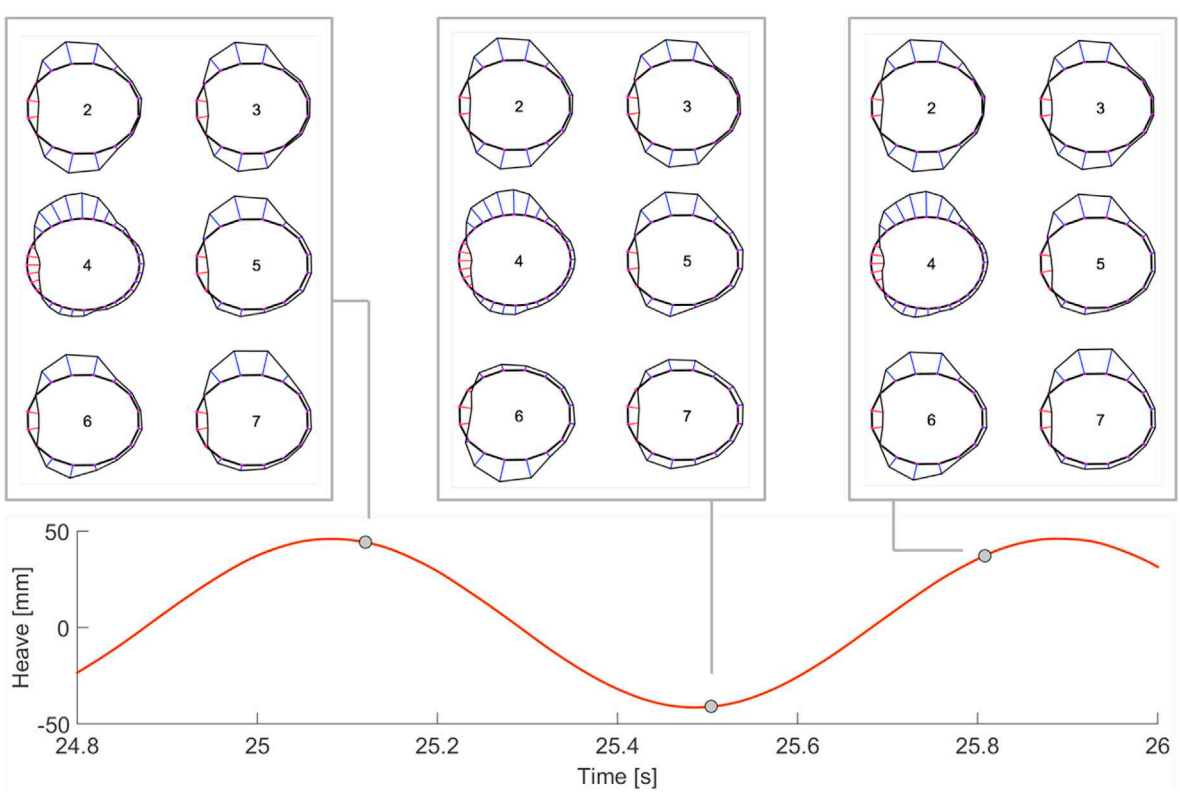

Fig. 12. Instantaneous pressure coefficients during a galloping event. $Sc_\zeta = 6.8$. Ring numbers are indicated at the centre of each cross-section.

segment of the cable. Sectional lift and drag coefficients in this manuscript have been normalized by the freestream wind speed and cable diameter. The fluctuations in lift are investigated in greater detail in this section to demonstrate the different excitation mechanisms in the critical and supercritical Reynolds number regimes.

5.1. Lift coefficient spectra

Tanaka et al. (2016) and Matsumoto et al. (2017) investigated the presence of low frequency fluctuations in the lift coefficient in the critical Reynolds number regime using a static cable model and related these observations to amplitude measurements recorded in a dynamic study with the same cable model. The current data set provided the unique opportunity to evaluate forces and response amplitude simultaneously on a dynamic model. In addition, the presence of several rings of pressure taps on the IHI cable model allowed the axial development of the flow to be investigated in greater detail, compared to the integrated lift and drag measurements obtained from balance measurements with a static model.

5.1.1. Critical Reynolds number regime

The power spectral density of the lift coefficient was calculated for each ring of pressure taps at all Reynolds numbers. The lift coefficient spectra are shown for the medium damping case in Fig. 14. The lift coefficient spectra are plotted as a function of Reynolds number and

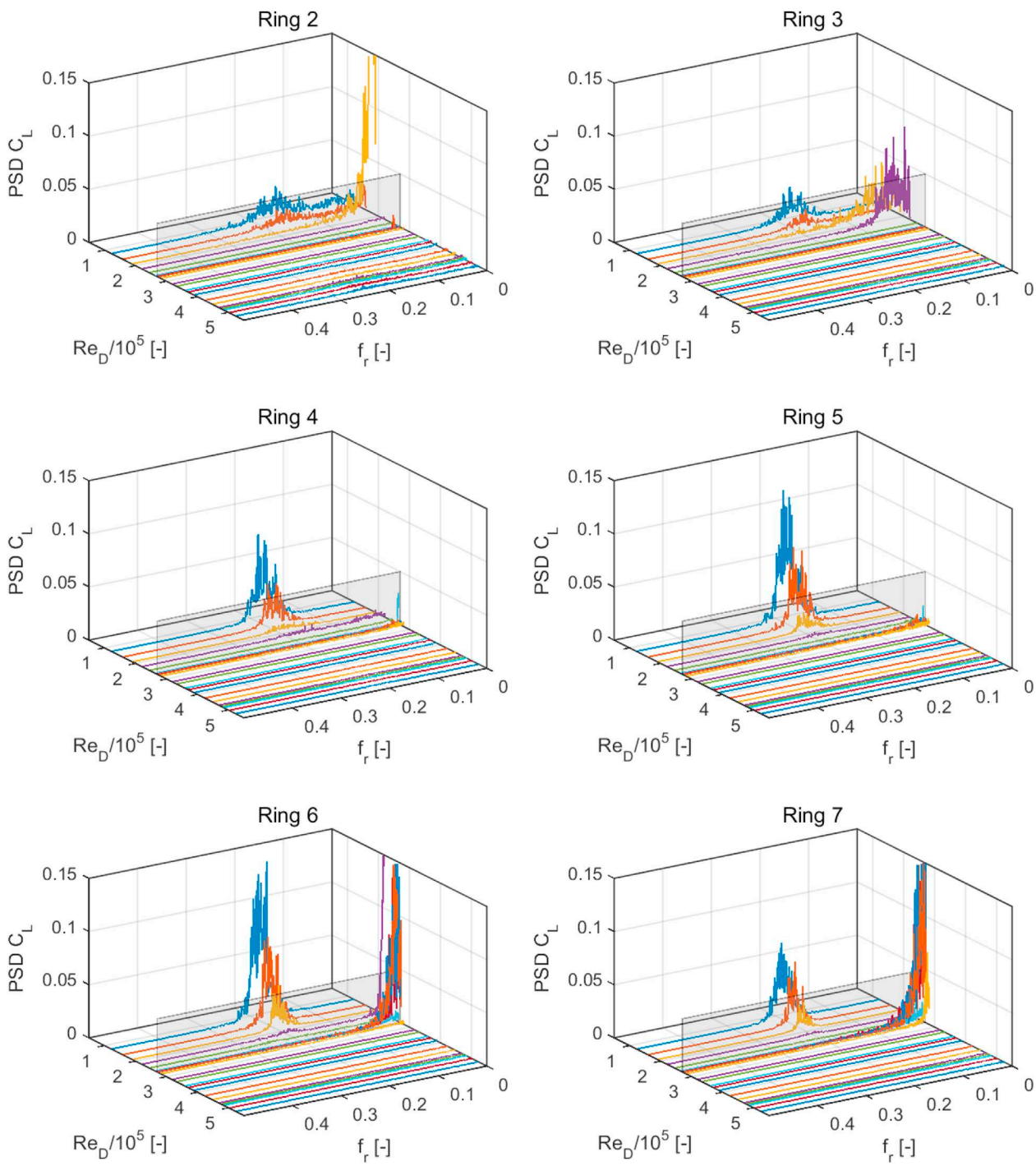

Fig. 14. Lift coefficient spectra for each ring of pressure taps. $Sc_\zeta = 6.8$.

reduced frequency $f_r = fD/U$, where f is the vector of frequencies in the lift coefficient spectra, D is the cable diameter, and U is the wind speed. Fig. 14 demonstrates several interesting flow features. Vortex shedding can be observed at all rings at low Reynolds numbers near a reduced frequency (Strouhal number) of 0.2. The vortex shedding is attenuated as the critical Reynolds number regime is approached. It is known that vortex shedding from a cylinder in cross-flow will experience a change in shedding behaviour in the critical Reynolds number regime. Additionally, vortex shedding attenuation has been linked to the development of axial flow on an inclined cable in Matsumoto et al. (2001). Vortex shedding is first attenuated on the upper rings of the cable and the attenuation occurs progressively in the spanwise direction on Rings 5, 6, 7 at higher Reynolds numbers. The vortex shedding was attenuated along the entire span of the cable at a Reynolds number of approximately 200, 000. Following the attenuation of vortex shedding on each ring, significant low frequency components appears in the lift spectra at reduced frequencies below 0.05. These low frequency components appear in the critical Reynolds number regime, between Reynolds numbers of 200,000 and approximately 280,000, depending on the spanwise position. The Reynolds number corresponding to the observation of cable galloping is indicated by the shaded, transparent plane overlayed on the spectra. Similar flow features were observed in the low damping data, which included fewer steps between Reynolds numbers near the onset of galloping.

Low frequency fluctuations had been observed in Matsumoto et al. (2017) in lift data obtained from balance measurements. Similar low frequency fluctuations were observed in the current work in the critical Reynolds number regime prior to and during the onset of dry galloping. These fluctuations are investigated in greater detail in Fig. 15, which plots the same lift coefficient spectra, but limited to a range of frequencies from 0 to 5 Hz. A secondary axis is included in Fig. 15 to plot the equivalent values of reduced frequency. The results for $Sc_\zeta = 6.8$ in Fig. 15 demonstrate that significant low frequency content appears in the critical Reynolds number regime as the galloping condition is approached. The cable oscillation frequency can be identified by the peak at 1.2 Hz for the spectra corresponding to 18.1 m/s. Low frequency content appears at 17.8 m/s and 18.1 m/s, at which point galloping occurred for $Sc_\zeta = 6.8$. As soon as the wind speed increases to 18.7 m/s, which is beyond the galloping condition, stable low pressure lobes appeared in the pressure data (Fig. 9) and the low frequency content was no longer apparent. Three of the sets of spectra shown in Fig. 15 are

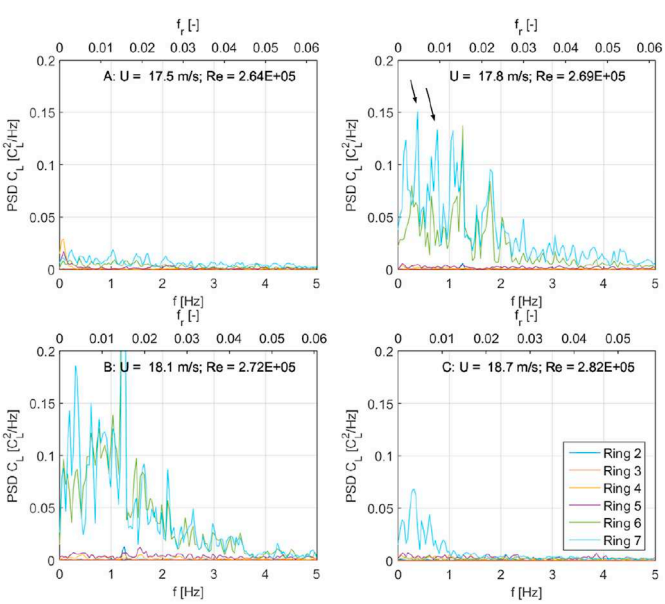

Fig. 15. Lift coefficient spectra at low frequencies in the critical Reynolds number regime. Smooth cable. $Sc_\zeta = 6.8$.

identified with a letter (A, B, C). These correspond to wind speeds and conditions, along with an additional point D at 21.2 m/s (not shown in Fig. 15), that will be discussed below in Figs. 17 and 20. The two peaks identified by arrows in the spectra at 17.8 m/s in Fig. 15 will be analyzed in the subsequent paragraphs.

The low frequency content exhibits peaks representing a concentration of oscillation energy at reduced frequencies that range from 0.002 to 0.01. Fluctuations in lift were observed over a similar range of reduced frequencies in the cable experiment of Matsumoto et al. (2017). It had been suggested by Matsumoto et al. (2017) that cables and other bluff bodies may undergo a process analogous to stall on an airfoil and that the physical process on a bluff body would involve sudden changes in Strouhal number, drag, lift, and the appearance of low frequency fluctuations in lift that create a stall-like state on a bluff body that destabilizes the laminar separation bubbles. The presence of low frequency fluctuations on airfoils prior to stall has been established in literature (Hain et al., 2009; Almutairi and AlQadi, 2012). Large Eddy Simulations of a NACA 0012 airfoil by Almutairi and AlQadi (2012) identified low frequency oscillations with reduced frequencies ranging from 0.0048 to 0.0062 and that these occurred over a small range of angles of attack prior to stall. These oscillations were associated with the formation, bursting, and flapping of the laminar separation bubble on the upper surface of the airfoil. Similarly, airfoil experiments by Hain et al. (2009) used time-resolved particle image velocimetry in a water channel to identify fluctuations at reduced frequencies ranging from 0.006 to 0.1 and these peaks were associated with the flapping of the boundary layer.

The unsteady pressure measurements in the current campaign have been used to confirm that the low frequency peaks in the lift coefficient spectra are in fact due to fluctuations in the suction peak of the pressure distribution, which can indicate a fluctuation in the laminar separation bubble. The peaks identified with arrows at 17.8 m/s for Ring 7 in Fig. 15 have reduced frequencies of 0.0047 and 0.0094. These correspond to fluctuations that last 2.6 s/cycle and 1.3 s/cycle, respectively. A time segment of 2.6 s was divided into 10 equal intervals, and the C_P data were averaged over each time interval. The pressure coefficients along the starboard surface of Ring 7 are shown in Fig. 16 as a function of non-dimensionalized arc length (arc length x divided by semi-circumference C) at the 10 averaged time intervals. The suction peak in the pressure distribution is shown to grow and shrink on the starboard surface of the cable over the cycle of 2.6 s. The interval-averaged time history of the pressure coefficients at $x/C = 0.43$, corresponding to the peak C_P observed in the data, is shown in Fig. 16, at right. This demonstrates the full cycle of the pressure distribution fluctuation over 2.6 s ($f_r = 0.0047$), in addition to the second, shorter fluctuation that has a cycle length of 1.3 s ($f_r = 0.0094$).

The range of reduced frequencies corresponding to the low frequency fluctuations in the current cable experiment, the experiment of Matsumoto et al. (2017), and airfoil stall are all consistent and appear to be associated with the dynamics of the pressure distribution caused by changes in the laminar separation bubble. A key difference between a cylinder and an airfoil is that an airfoil will only form a laminar separation bubble on the upper surface, whereas a cylinder can have laminar separation bubbles on one or both sides and these can also fluctuate from side to side.

A relationship was identified between the maximum peak in the power spectral density for the static lift coefficient and the amplitude from dynamic measurements by Matsumoto et al. (2017). In the current work, the root-mean-square (RMS) of the lift coefficient ($C_{L,RMS}$) was calculated at each Reynolds number, but was windowed over the range of frequencies from 0 to 5 Hz. The $C_{L,RMS}$ was calculated at each ring of pressure taps to establish the range of fluctuations in lift that were being experienced by the cable at any given Reynolds number. The mean C_L, mean C_D, amplitude, and $C_{L,RMS}$ are shown as a function of Reynolds number for the low and medium damping cases in Fig. 17. The maximum and minimum $C_{L,RMS}$ considering the data from Rings 2 to 7 are

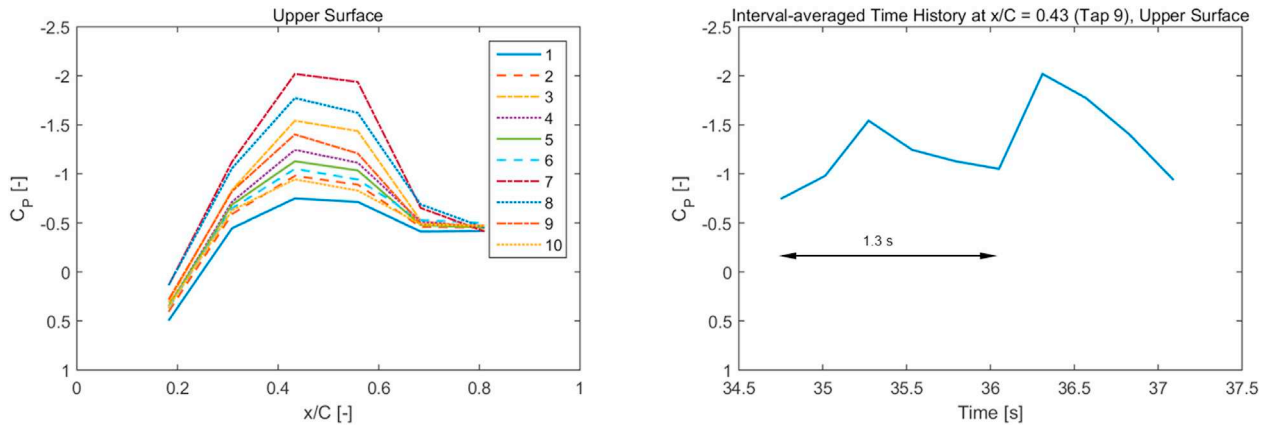

Fig. 16. Fluctuations in the low pressure lobes corresponding to reduced frequencies of 0.0044 and 0.0094. $Sc_\zeta = 6.8$, Ring 7, $Re = 269{,}000$.

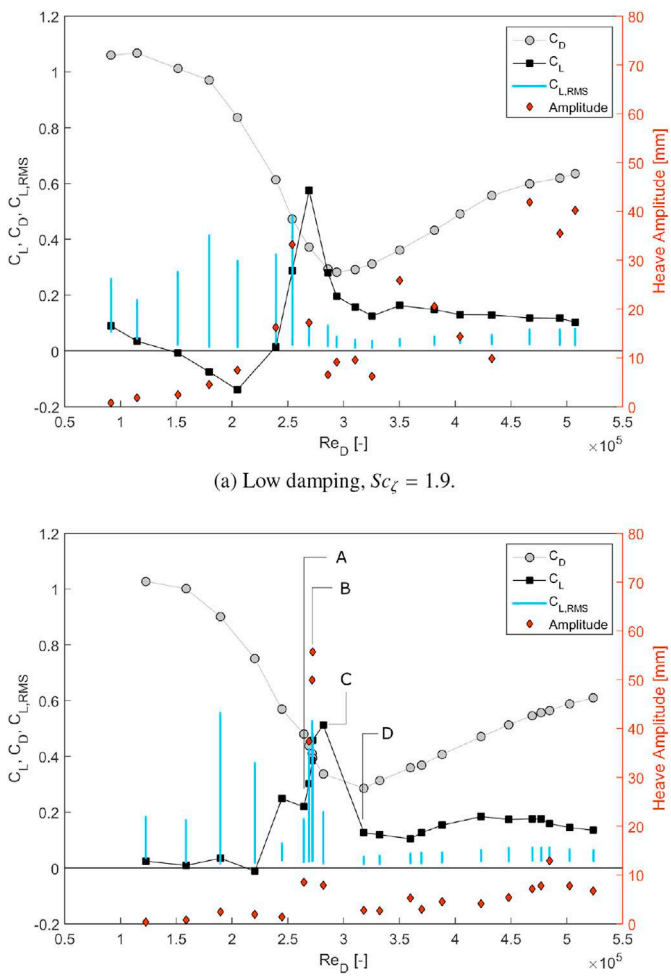

(a) Low damping, $Sc_\zeta = 1.9$.

(b) Medium damping, $Sc_\zeta = 6.8$.

Fig. 17. Comparison between amplitude, force coefficients, and lift rms. The data points identified correspond to data shown in Figs. 15 and 20. A: immediately prior to the onset of galloping, 17.5 m/s; B: peak amplitude during galloping, 18.1 m/s; C: maximum mean lift coefficient, but low amplitude, 18.7 m/s; D: drop in mean lift coefficient and low amplitude, 21.2 m/s.

connected with a line at each Reynolds number to show the range of fluctuations that were present over the span of the cable. Additionally, the points labelled with letters (*A*, *B*, *C*) in Fig. 17 correspond to the data identified with the same letters in Fig. 15. Recall that spectra were not shown earlier in Fig. 15 for point *D*.

The maximum $C_{L,RMS}$ corresponds to the maximum amplitude that was observed, and this occurred in association with a drop in drag, but prior to the highest mean lift coefficient. The low frequency fluctuations that lead to the maximum $C_{L,RMS}$ represent an unstable flow regime, where the boundary layer states can fluctuate, as shown earlier in Figs. 11 and 12. These instabilities may allow the separation bubble(s) to be influenced by the cable motion, which could induce a synchronization between the fluctuations in the low pressure lobe(s) and the cable displacement during the galloping event (Point B in Fig. 17b). It was suggested by Matsumoto et al. (2017) that the locking-in of the separation bubble fluctuations with the cable motion may be one reason why this type of galloping (described as *stall-type* galloping by Matsumoto) may be extremely difficult to mitigate through damping alone. In the current experiment, damping levels greater than those required by the code were not able to fully attenuate the vibrations in the critical Reynolds number regime. The maximum lift coefficient occurred following the galloping event and corresponds to a stable, asymmetric TrBL2 flow regime over much of the cable, which corresponds to a large, steady lift force and a low heave amplitude (Point *C* in Fig. 17b). Although this point exhibits the largest steady lift force, the fluctuations in lift are reduced, which may be related to the reduction in response amplitude. Following the range of speeds that corresponded to galloping (Point *D* in Fig. 17b), the pressure distribution becomes more symmetric (TrBL2 and eventually TrBL3 above a Reynolds number of 400,000) and the lift coefficient drops to approximately 0.2. The relationship between large amplitude vibrations at high Reynolds numbers and the lift coefficient will be discussed in the next section.

5.1.2. Supercritical Reynolds number regime

Large amplitude motion had been observed in this experiment at low damping levels in the supercritical Reynolds number regime. The amplitudes of these motions were shown in Fig. 17a and were associated with a low $C_{L,RMS}$ compared to the $C_{L,RMS}$ values observed during dry galloping in the critical Reynolds number regime. Additionally, the mean pressure distributions shown earlier in Fig. 9 identified a forward shift in the separation point and the transition between the TrBL2 and TrBL3 flow regimes. Unlike the dry galloping in the critical Reynolds number regime, these vibrations at high Reynolds number were amplitude-limited and were successfully attenuated with an increase in damping. This type of large-amplitude motion has been described in literature as high reduced velocity vortex-induced vibration (Matsumoto et al., 2001, 2017; Cheng et al., 2008). Reduced velocity is defined as $U_r = U/(fD)$, where U is the wind speed, f is the vector of frequencies in the lift coefficient spectra, and D is the cable diameter. Note that $U_r = 1/f_r$.

It has been proposed by Matsumoto et al. (2017) that this type of vibration may be associated with an interaction between an axial vortex

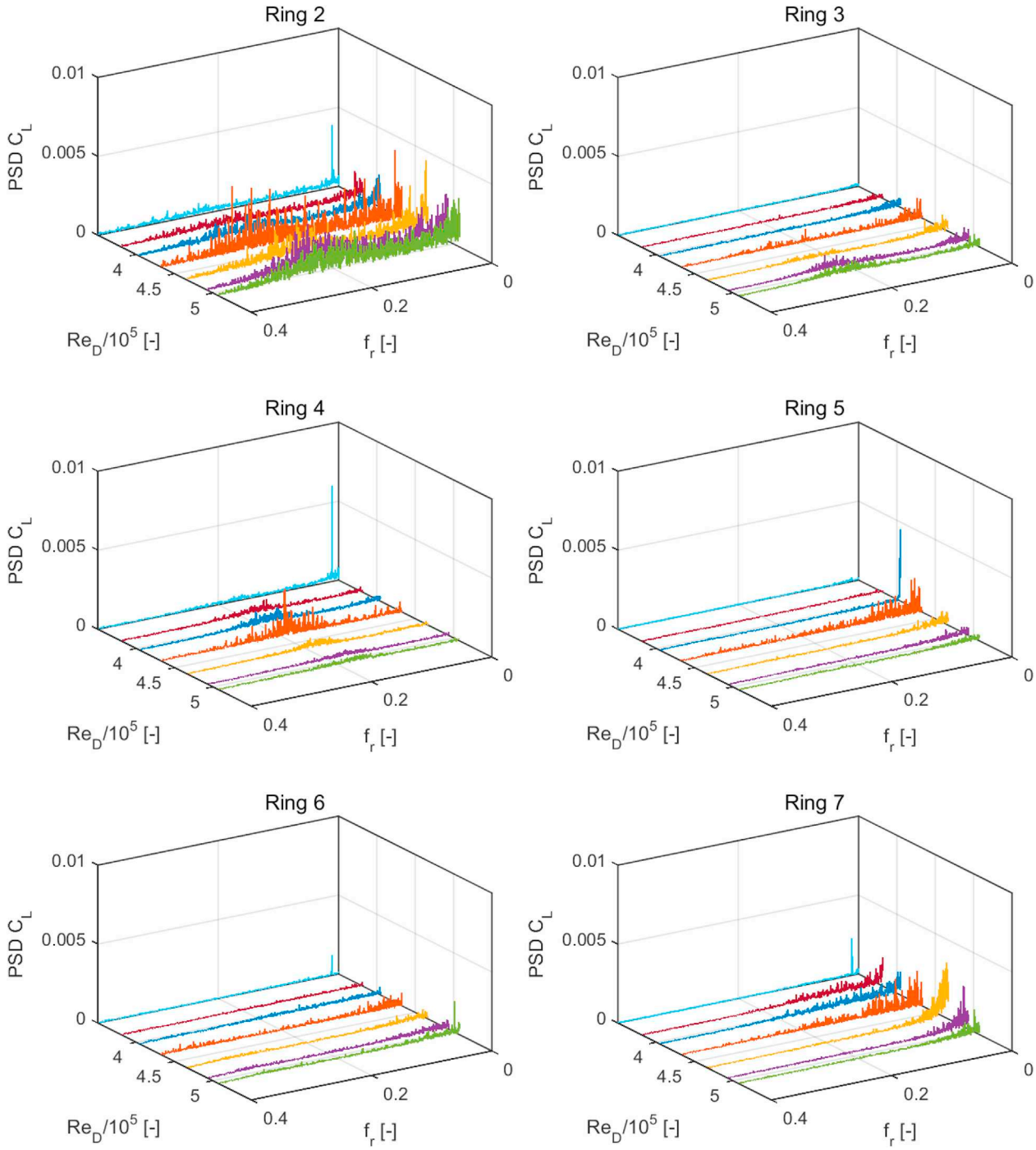

Fig. 18. Lift coefficient spectra at supercritical Reynolds numbers for each ring of pressure taps. $Sc_{\zeta} = 1.9$.

on the leeward side of the cable and Kármán vortex (K—V) shedding. It was shown through flow visualization at low speeds that the axial flow could interact with the K—V shedding to periodically generate an enhanced Kármán vortex at multiples of reduced velocity of 20 (Matsumoto et al., 2001). Although the flow visualization experiments in Matsumoto et al. (2001) were conducted at low Reynolds numbers, large-eddy simulations of inclined cables have confirmed the presence of a significant axial flow component in the critical Reynolds number regime and at supercritical Reynolds numbers (Hoftyzer, 2016). Vibrations that were observed at high Reynolds numbers in Matsumoto et al. (2017) were also linked to the presence of flow structures occurring at low frequencies that corresponded to reduced velocities in the range of 100.

The lift coefficient spectra shown earlier in Fig. 14 identified that K—V shedding was attenuated in the critical Reynolds number regime. Similar lift coefficient spectra data for the low damping case are shown in Fig. 18, but with axis limits that focus only on the high Reynolds number range. Note that the vertical axis range has been reduced to show a range of values that are 15 times smaller than those included in Fig. 14. An interesting feature of these spectra is that the K—V shedding that had been attenuated in the critical Reynolds number regime re-emerges at high Reynolds numbers at a reduced frequency of approximately 0.22. This is associated with an increase in the lift coefficient spectra at frequencies below a reduced frequency of 0.1 in Fig. 18. This confirms the presence of vortex shedding, in combination with low frequency content, that have been suspected in literature as causes of this type of large

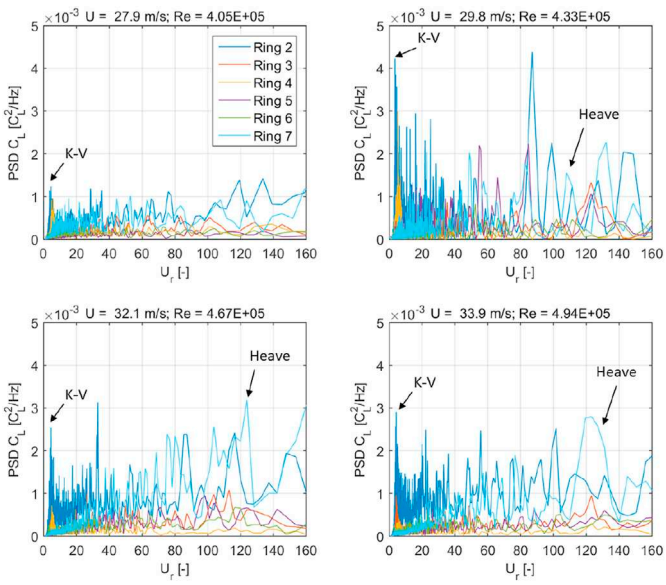

Fig. 19. Lift coefficient spectra at supercritical Reynolds numbers as a function of reduced velocity. $Sc_\zeta = 1.9$.

amplitude motion. It should be noted that the K—V shedding can be observed for Rings 2, 3, and 4, which are on the upper half of the cable. Similar vortex shedding was not observed in Fig. 18 on the lower half of the cable. It is possible that the observation of K—V shedding on only half of the cable, and the relative weakness of the fluctuation compared to the lift spectra in the critical Reynolds number regime, are factors that may allow this type of motion to be mitigated through additional damping.

The works of Cheng et al. (2008) and Matsumoto et al. (2017) described the presence of enhanced K—V shedding and lift fluctuations that may be present at multiples of reduced velocity of 20, in particular at reduced velocities that approach the frequency of cable oscillation. This is verified for the current results by plotting the lift spectra data for each ring as a function of reduced velocity in Fig. 19. The vibrations at high Reynolds numbers became apparent in this case at a wind speed of 29.8 m/s. The reduced velocities corresponding to K—V shedding (Strouhal number of 0.22) and to the cable oscillation frequency in heave are indicated in Fig. 19. It can be seen that several peaks are apparent near $U_r = 80$ and $U_r = 100$ that are approximately equal in magnitude to the K—V shedding. It is possible that these factors, along with the change in the boundary layer topology at high Reynolds numbers, may contribute to the large vibrations at high Reynolds numbers. Additionally, the relative weakness of the vortex shedding and spectral content at high reduced velocities, compared to the lift spectra in the critical Reynolds number regime, may be a significant factor in establishing why vibrations at high Reynolds numbers were easy to mitigate with additional damping.

5.2. Spanwise correlations

The factors associated with dry galloping in the critical Reynolds number regime were identified above as fluctuating laminar separation bubble behaviour, the appearance of low-frequency content in the lift coefficient spectra, and an increased $C_{L,RMS}$. The last factor investigated in this article is the correlation of the lift coefficient along the cable and its relationship with the amplitude. Increased spanwise lift correlation had been observed in the presence of dry galloping by ?

5.2.1. Critical Reynolds number regime

The time series of the lift coefficient for the entire cable was calculated by taking the sample-by-sample average of the lift coefficient from each ring of pressure taps. The overall lift coefficient and the heave displacement of the cable are plotted at four wind speeds in the critical Reynolds number regime in Fig. 20. The four wind speeds correspond to the points (A, B, C, D) that had been identified earlier in Figs. 15 and 17b. The fluctuations in C_L prior to the onset of galloping are shown for times series A, but these fluctuations are not synchronized with the cable displacement. When the cable is undergoing galloping (time series B), the large variations in the lift coefficient are synchronized with the heave displacement. The large changes in lift are driven by fluctuations in the low pressure lobes. The fluctuating surface pressures that had been shown earlier in Fig. 12 during the cable galloping event correspond to the time interval from 25 s to 26 s shown as part of time series B in Fig. 20. These fluctuations had identified that the boundary layer regime does not need to be consistent along the entire length of the cable, as long as the direction of the change in pressure is associated with the direction of displacement. Time series B in Fig. 20 identifies that these changes in pressure (and therefore lift) are correlated along the length of the cable and result in an overall lift coefficient that fluctuates with the cable displacement. The maximum lift coefficient occurs at a wind speed of 18.7 m/s (time series C) and is associated with a stable, asymmetric boundary layer regime. As the pressure distribution becomes more symmetric and more stable, C_L drops to approximately 0.1 in time series D.

The cross-correlation coefficient was calculated for the lift coefficient in order to characterize the large fluctuations that had been observed in the overall lift coefficient for the cable in time series B in Fig. 20. The cross-correlation coefficient was computed using the lift coefficient for each ring of pressure taps compared to Ring 4, which is located near the mid-span of the cable. It was expected that the remaining rings of pressure taps would be correlated strongly with Ring 4 at the wind speed corresponding to galloping. The cross-correlation coefficient for each ring relative to Ring 4 is plotted as a function of Reynolds number in Fig. 21. As the Reynolds number corresponding to dry galloping is approached, the cross-correlation coefficient approaches 1 along the entire span of the cable. The onset of galloping coincides to the Reynolds number where Rings 2, 3, 5, and 7 become highly correlated with Ring 4. This implies that the changes in pressure (and therefore, lift) are correlated along a distance of at least 12D. It should be noted that Ring 6 is negatively correlated with Ring 4 at the Reynolds number corresponding to galloping.

5.2.2. Supercritical Reynolds number regime

The correlation of the lift coefficient at high Reynolds numbers was evaluated in a similar manner to demonstrate the significant differences in the flow regime leading to large-amplitude vibration. The overall lift coefficient and the heave displacement of the cable are plotted at four wind speeds in the supercritical Reynolds number regime in Fig. 22 for the low damping case. Large amplitude vibrations were observed at the highest three wind speeds. In all cases, in spite of the large amplitude motion, C_L does not appear to exhibit the large, synchronized variations that were observed in the critical Reynolds number regime. The cross-correlation coefficient for each ring relative to Ring 4 is plotted as a function of Reynolds number in Fig. 23, in a similar manner to the cross-correlation coefficient for the $Sc_\zeta = 6.8$ case in the critical Reynolds number regime. This process was repeated for $Sc_\zeta = 1.9$ since large amplitude vibrations in the supercritical Reynolds number regime were only observed at the lowest damping level. At high Reynolds numbers, the lift coefficient at each ring is still highly correlated with the Ring 4 for all of the rings except Ring 7. As mentioned earlier, these types of vibrations, described in literature as high reduced velocity vortex shedding, have been linked by Matsumoto et al. (2017) to an interaction between K—V shedding and axial flow. However, this work demonstrates that a high degree of correlation along the length of the cable is also required for the motion to grow and persist.

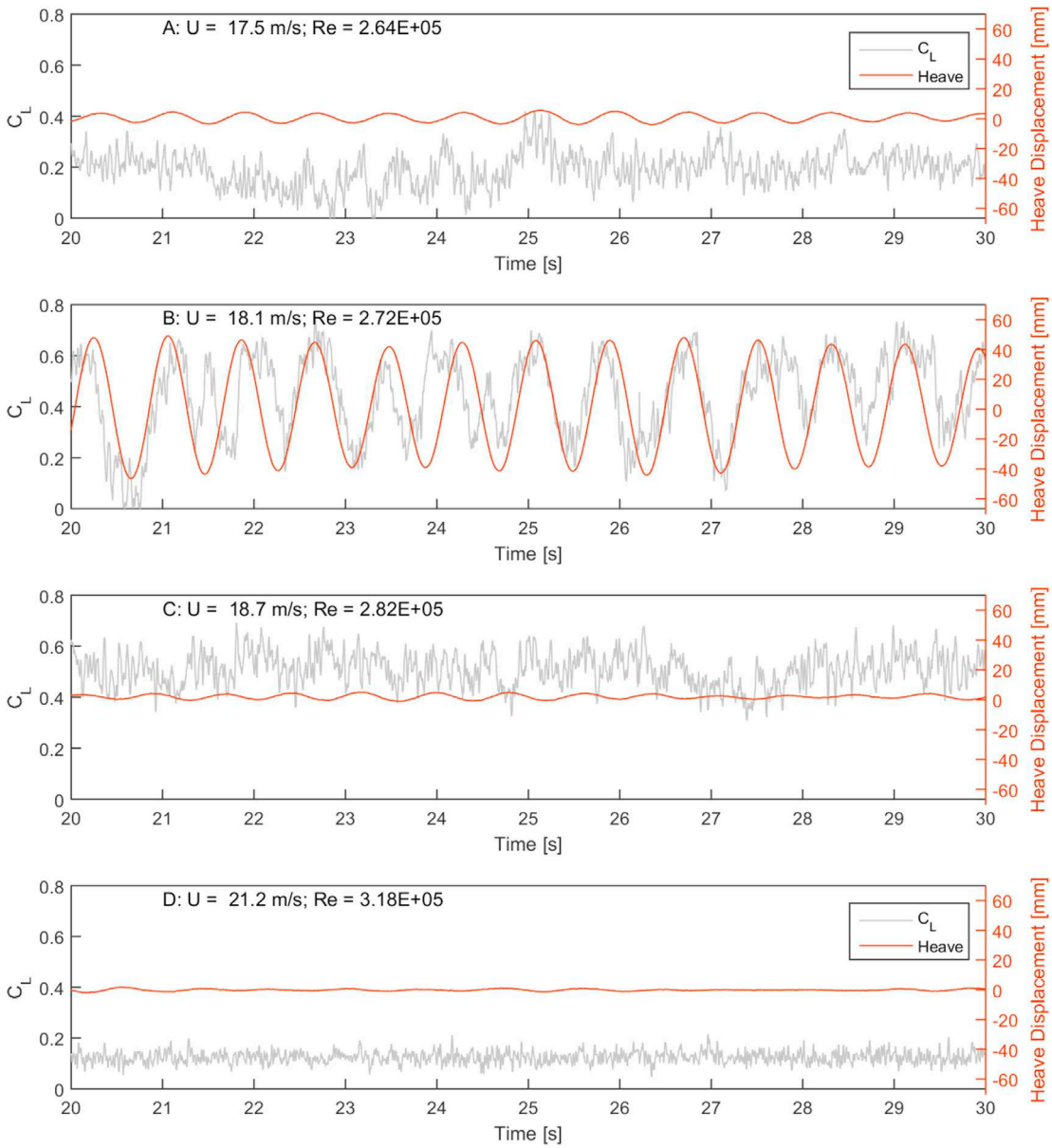

Fig. 20. Time history of heave displacement and lift coefficient. $Sc_{\zeta} = 6.8$. A: immediately prior to the onset of galloping, 17.5 m/s; B: peak amplitude during galloping, 18.1 m/s; C: maximum mean lift coefficient, but low amplitude, 18.7 m/s; D: drop in lift coefficient and low amplitude, 21.2 m/s.

6. Summary of vibrations and stabilization mechanisms

Two distinct types of large-amplitude vibrations were observed in the experiment and have been characterized in the current work. These two types of vibrations are:

- Dry galloping in the critical Reynolds number regime, associated with unbounded oscillations that could not be mitigated by damping levels higher than those required by bridge guidelines; and
- Large-amplitude vibrations at high Reynolds numbers, associated with bounded oscillations that could be attenuated with additional damping.

6.1. Critical Reynolds number regime

Several mechanisms were observed in the current work that contributed to the onset of dry galloping in the critical Reynolds number regime. The mechanisms contributing to the onset of dry galloping in the critical Reynolds number regime are summarized below:

- The mean drag dropped throughout the critical Reynolds number regime due to the appearance of one or two laminar separation bubbles on the cable surface.
- A sudden change in the lift distribution was observed due to one-sided or asymmetric low pressure lobes.
- Low frequency fluctuations appeared in the critical Reynolds number regime. These were associated with fluctuations in the laminar separation bubble and are believed to de-stabilize the pressure distribution on the cable. The fluctuations in pressure then become synchronized with the cable motion. The low frequency fluctuations in lift were characterized with $C_{L,RMS}$ windowed over frequencies from 0 to 5 Hz. A peak in $C_{L,RMS}$ was observed at the wind speed associated with galloping for the smooth cable.
- Several boundary layer states were present along the cable during galloping. It is believed that it is not a necessary requirement to have a correlation in the type of boundary layer state to drive galloping. However, a correlation in lift along the cable and a synchronization

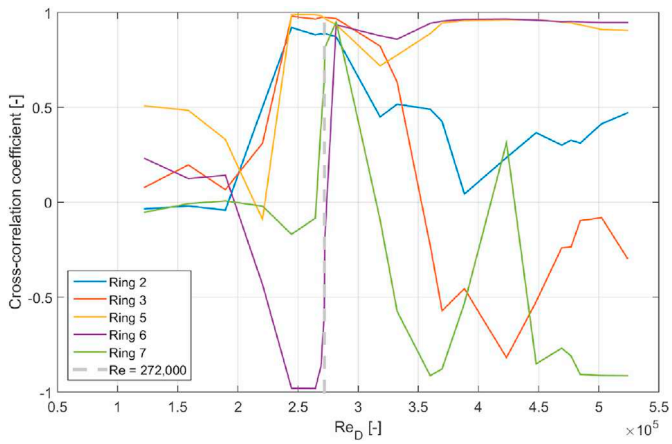

Fig. 21. Cross-correlation coefficients of the sectional lift coefficient at each ring compared to the lift coefficient at Ring 4. The dry galloping condition is indicated at a Reynolds number of 272,000. Smooth cable, $Sc_\zeta = 6.8$.

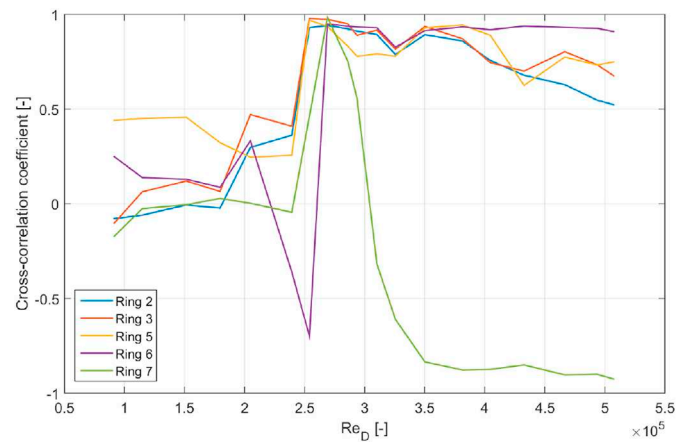

Fig. 23. Cross-correlation coefficients of the sectional lift coefficient at each ring compared to the lift coefficient at Ring 4. $Sc_\zeta = 1.9$.

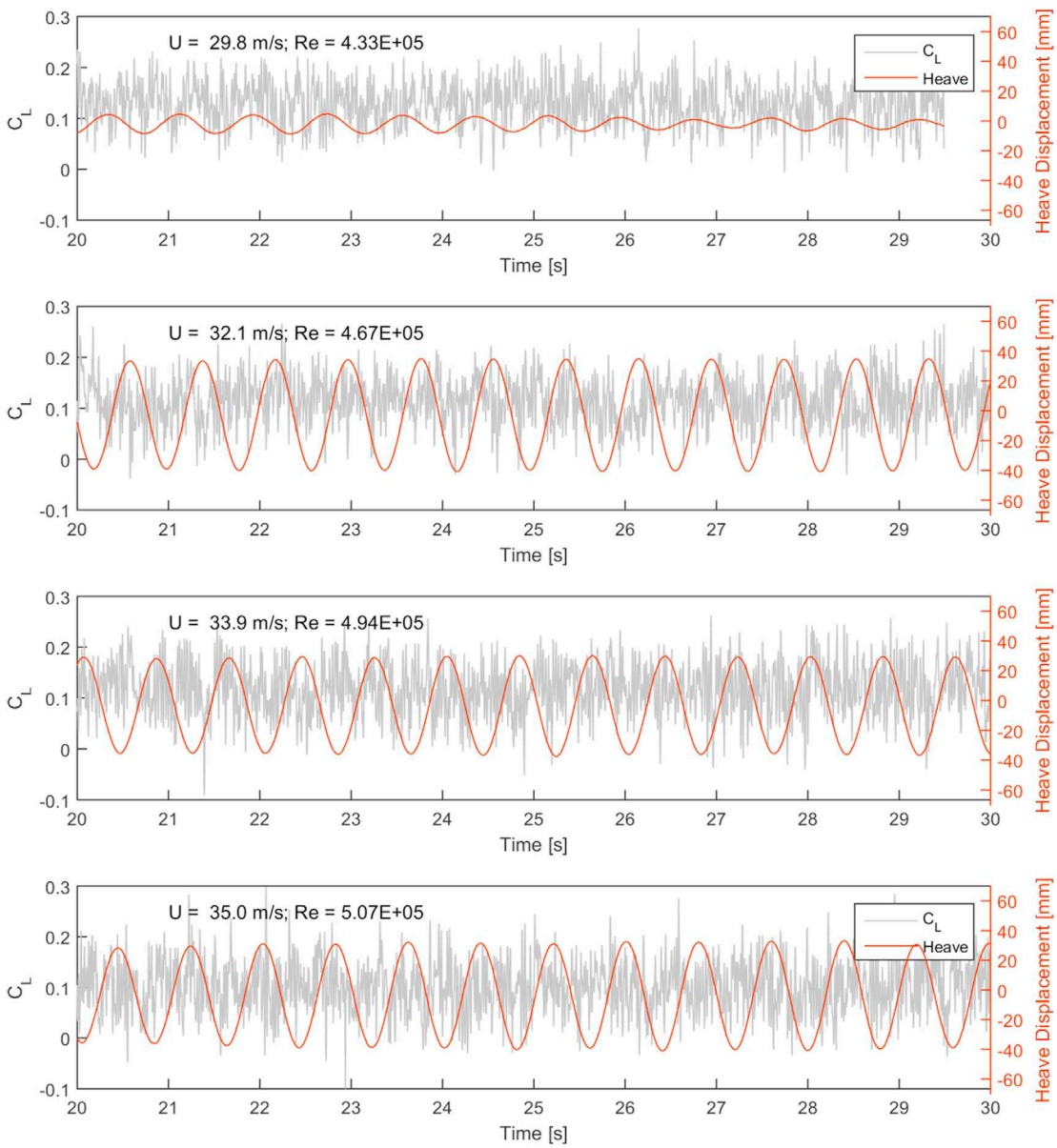

Fig. 22. Time history of heave displacement and the overall lift coefficient at high Reynolds numbers. $Sc_\zeta = 1.9$.

between the direction of the change in pressure and the cable displacement are important contributing factors to galloping. The locking-in of the low pressure lobe fluctuations and the cable displacement is one reason why it is believed that this type of dry galloping can be difficult to mitigate with damping alone.
- A high level of correlation in the lift coefficient was observed immediately prior to the onset of dry galloping.

6.2. High Reynolds numbers

The mechanisms leading to vibrations at high Reynolds numbers were shown to be different than those leading to galloping in the critical Reynolds number regime. The current work suggests that several factors contributed to the bounded oscillation observed at high Reynolds numbers:

- The boundary layer state changed prior to the development of large-amplitude vibrations at high Reynolds numbers. The separation point shifted forward, and a boundary layer state resembling the onset of the TrBL3 regime was present, with an asymmetric pressure distribution on the port and starboard sides of the cable.
- Kármán vortex shedding re-emerged at high Reynolds numbers. This may be associated with additional shedding frequencies at high reduced velocities (low reduced frequencies) that occur at similar reduced velocities as the cable oscillation. The K—V shedding and the low frequency fluctuations had a magnitude that was 10 times smaller than the fluctuations observed in the critical Reynolds number regime, which is why this type of oscillation may be easily mitigated with additional damping.
- The lift coefficient was still highly correlated along most of the cable at high Reynolds numbers.

7. Conclusions

Experiments were conducted for IHI Corporation on a 1:1 scale sectional model of a stay cable in the 3 m°×°6 m Wind Tunnel at the NRC in 2015. Dry-state galloping was observed for a smooth cable in a low damping configuration and large amplitude vibrations were still observed in the critical Reynolds number regime at damping levels up to a Scruton number of $Sc_\zeta = 13.8$, which corresponded to damping levels greater than those recommended by the Post-Tensioning Institute ($Sc_\zeta = 10$). Additionally, large-amplitude vibrations were observed at high Reynolds numbers and these were easily mitigated with additional damping. The current manuscript provided a detailed investigation of the unsteady surface pressure data at multiple damping levels in the critical and supercritical Reynolds number regimes.

The current study identified several important factors that contributed to dry galloping and large-amplitude cable motions. It was shown that the physical mechanisms leading to the onset of large-amplitude motion in the critical and supercritical Reynolds number regimes are distinct. In the critical Reynolds number regime, the drop in drag, increase in lift, and fluctuations in the laminar separation bubbles along the cable destabilize the low pressure lobes, allowing the changes in pressure along the cable to become synchronized with the cable motion in a highly-correlated manner. This type of galloping could not be mitigated with damping greater than that required by the PTI, but could be attenuated with the use of a helical fillet. At high Reynolds numbers, Kármán vortex shedding re-emerged and appeared to combine with low-frequency variations to induce large-amplitude motion that could be mitigated with additional damping.

Acknowledgements

The current study was funded by Infrastructure Canada as part of the Climate-Resilient Buildings and Core Public Infrastructure project. The authors would like to thank the technical support team in the NRC Aerodynamics Laboratory for their assistance.

References

Almutairi, J., AlQadi, I., 2012. Large eddy simulation of natural low-frequency oscillations of separating-reattaching flow near stall conditions. In: Proc. Of the 42nd AIAA Fluid Dynamics Conference and Exhibit. No. AIAA 2012-2698.
Benidir, A., Flamand, O., Gaillet, L., Dimitriadis, G., 2015. Impact of roughness and circular-defect on bridge cables stability. J. Wind Eng. Ind. Aerod. 137, 1–13.
Cheng, S., Larose, G., Savage, M., Tanaka, H., Irwin, P., 2008. Experimental study on the wind-induced vibration of a dry inclined cable - part I: Phenomena. J. Wind Eng. Ind. Aerod. 96, 2231–2253.
D'Auteuil, A., 2010. Manipulation of the Boundary Layer Transition to Enhance the Aerodynamic Performance of Athletes (ph.d thesis).
ESDU, 1971. Fluid Forces on Non-streamline Bodies-background Notes and Description of the Flow Phenomena, item 71012.
Hain, R., Kähler, C., Radespiel, R., 2009. Dynamics of laminar separation bubbles at low-Reynolds-number aerofoils. J. Fluid Mech. 630, 129–153.
Hoftyzer, M., 2016. Aerodynamic Characteristics of Yawed Inclined Circular Cylinders ph.d thesis.
Jakobsen, J.B., Andersen, T.L., Macdonald, J.H., Nikitas, N., Savage, M.G., McAuliffe, B.R., 2009. Wind tunnel testing of an inclined aeroelastic cable model - pressure and motion characteristics, Part II. In: Proc. Of 5th European African Conference on Wind Engineering, Florence, Italy, July 19-23.
Larose, G.L., D'Auteuil, A., 2014. Wind Tunnel Investigations of an Inclined Stay Cable with a Helical Fillet. Tech. Rep. FHWA-HRT-14-070. Federal Highway Administration.
Matsumoto, M., Yagi, T., Shigemura, Y., Tsushima, D., 2001. Vortex-induced cable vibration of cable-stayed bridges at high reduced wind velocity. J. Wind Eng. Ind. Aerod. 89, 633–647.
Matsumoto, M., Ishizaki, H., Tanaka, T., 2017. Rain and wind induced vibration and dry galloping of stay cables - its mechanism and aerodynamic stabilization. In: Proc. Of the International Symposium on the Dynamics and Aerodynamics of Cables (ISDAC 2017), Porto, Portugal, October 30-31, pp. 13–37.
Nikitas, N., Macdonald, J., 2015. Aerodynamic forcing characteristics of dry cable galloping at critical Reynolds numbers. Eur. J. Mech. B Fluid 49, 243–249.
Nikitas, N., Macdonald, J.H., Andersen, T.L., Jakobsen, J.B., Savage, M.G., McAuliffe, B.R., 2009. Wind tunnel testing of an inclined aeroelastic cable model - pressure and motion characteristics, part I. In: Proc. Of 5th European African Conference on Wind Engineering, Florence, Italy, July 19-23.
PTI Guide Specification, 2012. Recommendations for Stay Cable Design, Testing and Installation dc45.1-12. Tech. rep, sixth ed. Post-Tensioning Institute Committee on Cable-Stayed Bridges.
Tanaka, T., Matsumoto, M., Ishizaki, H., Kibe, H., 2016. Stall-type galloping and its aerodynamic stabilization of stay-cables of cable-stayed bridges. In: Proc. Of the 8th International Colloquium on Bluff Body Aerodynamics and Applications.
Yamauchi, K., Uejima, H., McTavish, S., Larose, G., 2016. Effects of a helical fillet on the wind-induced response of bridge cables in dry conditions. In: Proc. Of the 8th International Colloquium on Bluff Body Aerodynamics and Applications.
Zdravkovich, M.M., 1997. Flow Around Circular Cylinders, vol. 1. Oxford University Press, Oxford, UK.